JOURNAL OF GEOPHYSICAL RESEARCH, VOL. 112, C05013, doi:10.1029/2006JC003725, 2007

Alongshore currents and mesoscale variability near the shelf edge off northwestern Australia

K. H. Brink,[1] F. Bahr,[1] and R. K. Shearman[2]

Received 22 May 2006; revised 20 September 2006; accepted 21 November 2006; published 5 May 2007.

[1] Shelf break conditions and alongshore flow off northwestern Australia are studied during the strongly evaporative conditions of austral winter 2003. Present results, along with those of previous authors, confirm that a poleward, fresh Leeuwin current core is normally found near the shelf break. Salinity increases alongshore toward the southwest. Although there is no obvious shelf break front, there is a persistent offshore upward tilting of isopycnals in the depth range of 100–150 m. Repeated mesoscale surveys were made at the shelf edge during 8 days when the shelf break flow was equatorward. Waters offshore of the shelf break contain a rich baroclinic ageostrophic eddy field, with typically 10 km length scales, and the eddy patterns in the upper 60 m are uncorrelated with those below 90 m. The two depth horizons yield energy transfers from mean to eddy potential energy and appear to represent distinct finite amplitude instabilities on upper ocean and 180 m mean velocity cores, respectively. A linear stability model supports the existence of the two vertically separated instability types.

Citation: Brink, K. H., F. Bahr, and R. K. Shearman (2007), Alongshore currents and mesoscale variability near the shelf edge off northwestern Australia, *J. Geophys. Res.*, *112*, C05013, doi:10.1029/2006JC003725.

1. Introduction: Large-Scale Context

[2] Continental shelf and neighboring waters off northwestern Australia (Figure 1) have generally westward or southwestward flow patterns associated with the Indian Ocean South Equatorial Current and the headwaters of the poleward, shelf edge Leeuwin Current [e.g., *Church and Craig*, 1998]. During the austral winter, winds are relatively weak while warm, dry air associated with the nearby deserts drives evaporative processes over the shelf. The oceanic effects of this evaporation can be quite dramatic [e.g., *Holloway*, 1995], with dense salty water becoming especially pronounced on the inner part of the shelf. During the austral summer, conditions are more humid, and dramatic wind-forcing events occur in the form of very energetic atmospheric cyclones [*Church and Craig*, 1998]. Tidal currents are extremely energetic in this area, and have been well studied, especially with regard to the internal tides, which are quite dramatic near the shelf edge during the austral summer, when waters in the upper 50 m are relatively well stratified [e.g., *Holloway*, 1994]. Although clearly much is already known about this region, most of the oceanographic information was obtained either by means of moorings or relatively broad scale, nonrepeating hydrographic surveys.

[3] Prior approaches have left a number of questions about this region. One general concern is about processes near the shelf edge; for example, does the Leeuwin Current have a continuous, steady, stable core? Or does it show signs of instabilities and complex shelf edge eddies and meanders, as are found in other regions, such as south of New England [e.g., *Garvine et al.*, 1988]? Further, the existence of strongly evaporative conditions over the shelf provides a nearshore source of dense water that appears analogous to that formed over the shelf at high latitudes in response to wintertime cooling [e.g., *Cavlieri and Martin*, 1994]. If this is the case, then the expected instabilities and cross-shelf eddy buoyancy transports [e.g., *Pringle*, 2001] could be studied far more conveniently in the benign Australian conditions than during the winter at higher latitudes.

[4] We thus set out to study the waters off the northwest coast of Australia during June–July 2003, making heavy use of towed undulating sampling systems that allow highly resolved (0.1–2 km horizontal resolution, depending on the water depth), synoptic measurements of hydrography and currents. We focus on the detailed, three-dimensional spatial structure of shelf edge processes, and on middle to inner shelf spatial structures associated with shelf water densification. Our results are diverse, and so will appear through several publications. We focus here on the time variation of alongshore flow, large-scale processes and eddy observations near the shelf edge. *Brink and Shearman* [2006] concentrate on a coherent subsurface saltwater tongue, extending offshore from the shelf edge, and on its implications. Further, *Shearman et al.* [2004] treat detailed measurements in the eddy rich middle to inner shelf area, and their relation to existing ideas about buoyancy-driven exchanges.

2. Observations and Methodology

2.1. Overview

[5] The research cruise departed Port Hedland on 18 June and ended at Darwin (Figure 1) on 17 July 2003. The first

[1]Woods Hole Oceanographic Institution, Woods Hole, Massachusetts, USA.
[2]College of Oceanic and Atmospheric Sciences, Oregon State University, Corvallis, Oregon, USA.

0148-0227/07/2006JC003725$09.00

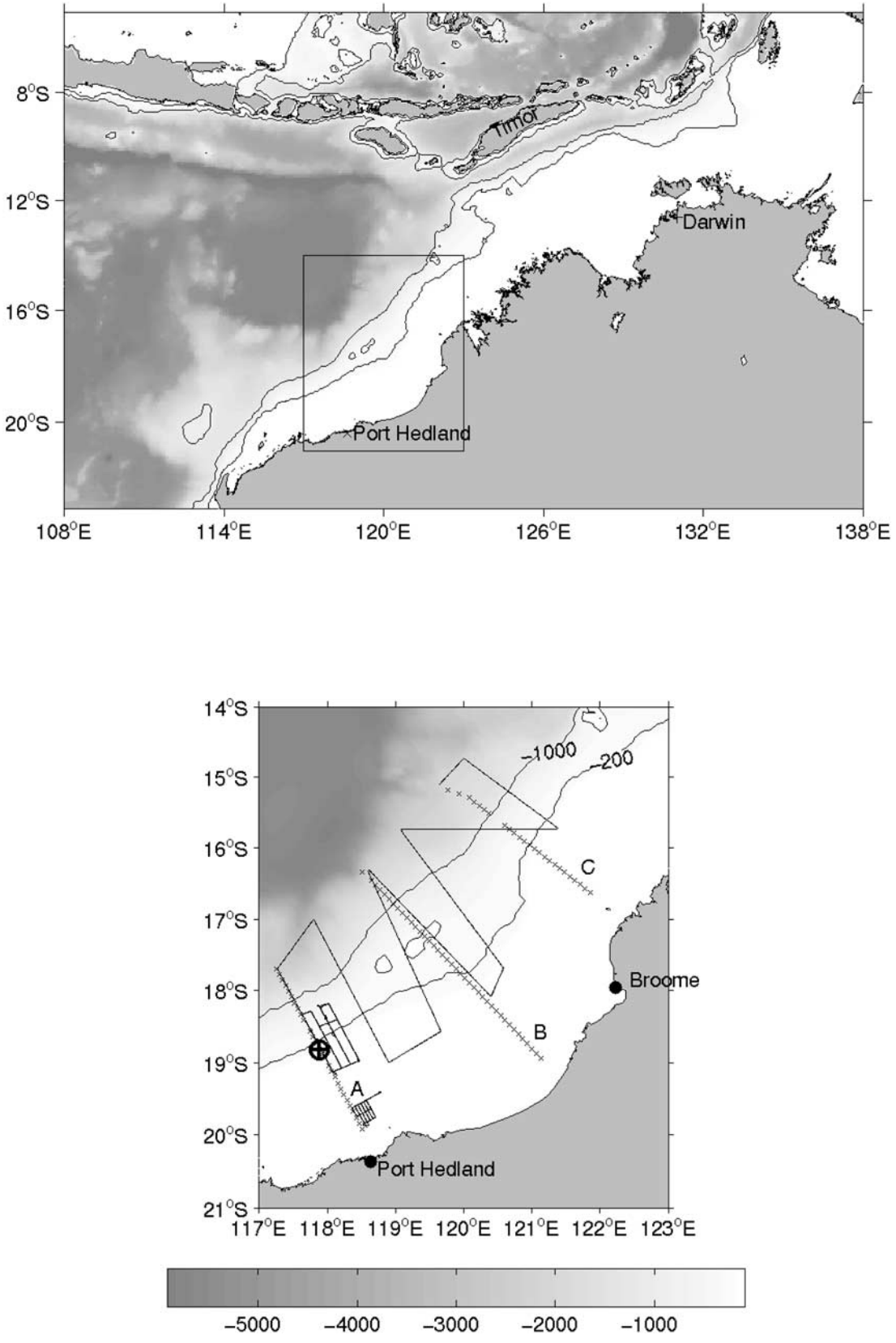

Figure 1. Locator map of the study area. (top) Regional scale showing the 200 m and 1000 m isobaths. (bottom) Detailed sampling region. Crosses are the locations of CTD stations, and the large, circled cross is the location of the current meter mooring. Solid lines denote SeaSoar sampling lines, except for the small grid on the inner shelf that denotes MiniBat sampling [*Shearman et al.*, 2004].

week of the cruise involved a three-line CTD survey to establish the context over 100 s of km and to depths greater than the 200 m sampled by our towed undulating samplers. On 18 June, we deployed an Acoustic Doppler Current Profiler (ADCP) mooring at the 144 m isobath along the first cross-shelf line. This mooring provided critical temporal context for our other measurements (see section 3). The CTD survey was followed by a better-resolved broad-scale SeaSoar survey (Figure 1, bottom) ending near the mooring location. This one-week survey provided better detail along with some replication for the CTD sections. Next, six repeated SeaSoar maps of shelf edge variability were conducted near the mooring in order to establish the temporal and spatial patterns in shelf edge processes. Each map took about 1.5 days to complete, and extended from the 80 m isobath offshore to about 45 km beyond the 200 m isobath, for a typical line length of about 100 km. Finally, finely resolved Minibat surveys were conducted, generally inshore the 50 m isobath, to study spatial patterns associated with evaporative forcing over the inner shelf [see *Shearman et al.*, 2004]. Shipboard meteorological measurements were made continuously throughout the cruise.

2.2. Time Series Data

[6] An upward looking 300 kHz broadband ADCP was moored near the bottom at the 144 m isobath (18°49.8′S, 117°53.1′E) on 18 June and recovered on 14 July 2003. The data were initially averaged into 20 min profiles, consisting of 4 m (vertical) bins. The data were edited for quality and the upper 15% of the water column was dropped because of sidelobe considerations. The final data set thus spanned 19–131 m depth. The vector records were rotated 29.5° to follow the local along-isobath direction, with the *u, v* components in the alongshore (toward the northeast) and offshore directions, respectively. The data were also low-pass filtered with the PL64T filter [*Beardsley et al.*, 1983], having a half amplitude point of 33 hours.

[7] Coastal sea level and atmospheric pressure records were obtained from Darwin, Broome and Port Hedland (Figure 1). These were combined to compute adjusted sea level (ASL), which is the pressure actually felt by the ocean. In addition, land-based wind records were obtained from Broome and Darwin. All of these records were also low-pass filtered with the PL64T filter. Our best estimates of wind stress amplitudes in the area are based on the shipboard underway meteorological measurements, which yield a mean wind stress 0.04 Pa toward 309°T, and major (minor) axis standard deviation of 0.05 (0.02) Pa toward 296°T.

2.3. ADCP Data Underway

[8] The R/V *Melville* was equipped with a hull-mounted 150 kHz narrowband ADCP. This system was interfaced with a Global Positioning System (GPS) navigation system and a differential GPS heading sensor system (“Ashtech”). Data were collected as 5 min ensembles in 8 m (vertical) bins. The data were processed using the Common Oceanographic Data Access System (CODAS) software [*Firing et al.*, 1995]. Several methods were tried to remove the energetic barotropic tides from the ADCP records. In our case, the best method uses the moored ADCP data to estimate the depth-integrated M_2 tides at that location, and then assumes that the same tidal transports apply everywhere. The underway ADCP data failed to reveal any appreciable alongshore variation in the M_2 phase within our region (sea level M_2 tides at Broome and Port Hedland tides are in phase to within 17 min). Similarly, *Clarke* [1991] did not find any alongshore phase variation over this area in coastal sea level. The suitability of our tide removal is confirmed by a reduction of current variability (standard deviation of depth-integrated currents decreasing by 42% over the entire underway ADCP record) and by visual inspection. For comparison with the depth-averaged tide of 0.26 m/s, the phase-locked component of the internal tide at the mooring location is 0.09 m/s or less (depending on depth).

2.4. In Situ Data

[9] The SeaSoar towed undulating platform generally operated between the surface and about 200 m of water. In shallower water (as shallow as 75 m), it operated to within 5–10 m of the bottom. The ship traveled at about 8 knots, and cycle time for a SeaSoar undulation was typically 2–7 min. The SeaSoar vehicle was equipped with sensors for temperature (two sensors), conductivity (two sensors), pressure, chlorophyll fluorescence, yellow matter fluorescence, light transmission, oxygen and bioluminescence. Only data from the temperature, conductivity and pressure sensors are reported on here. The temperature and conductivity sensors both received precruise and postcruise calibrations. Processing accounted for sensor lag times and for thermal lag [*Lueck*, 1990]. Quality control was conducted on 1-s averages of the 24 Hz raw data, and the clean data were then averaged in 2 m (vertical) bins, one for each up-down cycle. See http://science.whoi.edu/users/seasoar/vietnam/vanc11/ for further information. CTD data processing and quality control was carried out by shipboard technicians using standard SeaBird software.

[10] We estimate noise variances and correlation lengths scales for purposes of plotting and data analysis. We use the repeat SeaSoar radiator data to estimate these scales by means of isotropic structure function calculations as described by *Gawarkiewicz et al.* [2004]. For computing a space scale, data taken within 2 hours were treated as simultaneous. There were not enough data to create robust estimates of timescales. Spatial scales were found to vary considerably between depths and variables. For example, the temperature length scale is 15 km at 5 m depth but 8 km at 101 m depth, while the fluorescence length scale at 5 m is 10 km. We chose a conservative length scale of 10 km for all variables. Noise variances are 10% for SeaSoar data, and 15% for detided underway ADCP data.

3. Temporal Context

[11] The temporal context is established using the moored current meter records, since the mooring was placed in a representative position near the core of the shelf break alongshore flow. Tidal variability dominated the current meter records, but, for comparison with other data sets, we now consider only the low-pass-filtered currents (Figure 2). On the basis of work by *Holloway* [1995] for example, and other information about the Leeuwin Current, we had expected the mooring to detect predominantly southwestward (poleward) alongshore flow at this location.

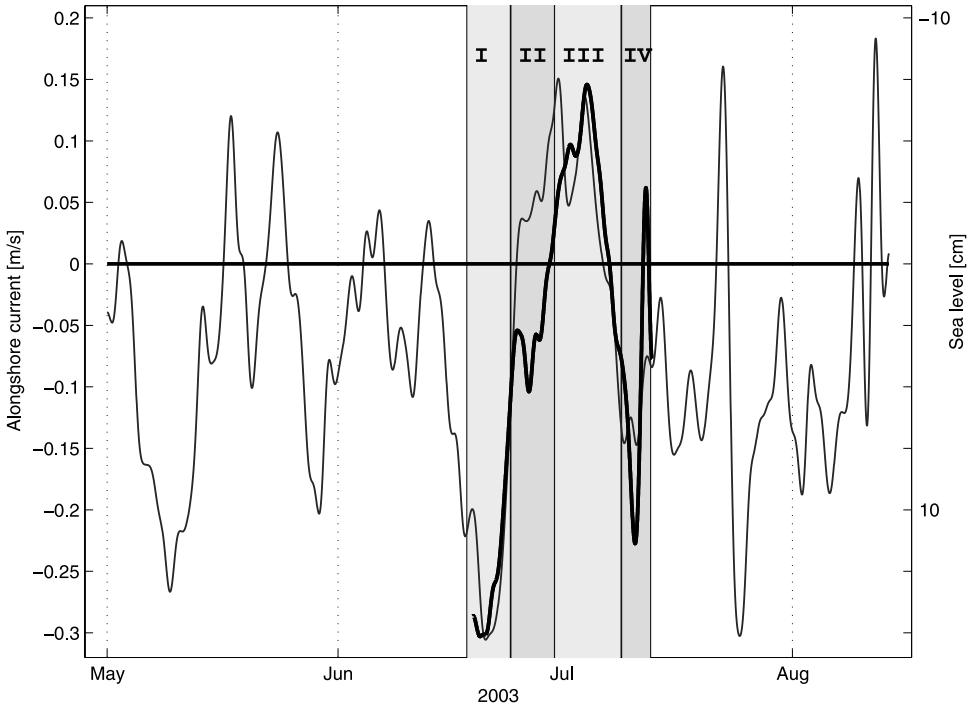

Figure 2. Time series of low-pass-filtered alongshore velocity (thick solid line, positive values toward 29.5° north of east) and adjusted coastal sea level at Port Hedland (thin solid line). The shaded areas represent different phases of our sampling: I is the large-scale CTD survey, II is the large-scale SeaSoar survey, III is the SeaSoar repeat radiator survey, and IV is the period of MiniBat sampling.

Indeed, this flow occurred initially, during the CTD operations and most of the large-scale SeaSoar survey, but the alongshore flow reversed to equatorward for 9 days starting around 1 July, thus spanning most of the period of shelf edge repeat radiator surveys. The flow then returned to poleward conditions for most of the remainder of the cruise.

[12] We ask whether equatorward or poleward shelf edge flow is normal at this location over a seasonal timescale. This problem is addressed using the longer, nearby Port Hedland adjusted coastal sea level record, since, consistent with geostrophy, alongshore currents are well correlated with coastal adjusted sea level. Specifically, for the 24-day duration of the filtered current meter record, the currents and sea level are highly correlated (−0.78) at zero lag. The negative correlation is expected from geostrophy in an offshore decaying alongshore flow in the southern hemisphere. We then use regression to scale and overplot the two records (Figure 2). This plot suggests that poleward (Leeuwin Current sense) flow conditions are normal (75% of the time) over the duration of the austral winter, and that we had encountered the longest episode of equatorward flow during this seasonal window during the repeat SeaSoar shelf edge surveys.

[13] Where do the alongshore current fluctuations originate? Given that alongshore flow and adjusted coastal sea level (ASL) are well correlated, we use the longer (May–August, 2003) wintertime coastal adjusted sea level records from Port Hedland, Broome and Darwin. We restrict our attention to this time window in order to avoid seasonal nonstationarity. We also use alongshore wind stress records from Broome and Darwin. Broome ASL is correlated with local wind (−0.5 with alongshore wind stress, where ASL lags wind stress by 8 hours) and Port Hedland ASL is also correlated with Broome wind stress (−0.5 to −0.6, depending on the definition of alongshore, with ASL lagging by 17–21 hours). All cited correlations in this section are nonzero with at least 95% confidence. Darwin (about 1600 km equatorward of our area) ASL is correlated with its local northward wind stress (−0.45 at 0 lag). Although Broome and Port Hedland ASL records are well correlated with each other (0.82, with Broome lagging by 0.5 days), neither record is significantly correlated with the Darwin ASL.

[14] For the Broome–Port Hedland area, these results are consistent if shelf conditions (current and sea level) are responsive to forcing by nearby alongshore winds, and if the weather systems propagate toward the northeast. This sense of weather system motion would account for Port Hedland ASL leading Broome's: the opposite sense to what might be expected from free coastal-trapped wave propagation. Darwin, which seems isolated, lies about 400–600 km east of the shelf break where it turns toward Timor, so we suspect that it is insulated from any shelf break (topographically trapped) waveguide, a conclusion consistent with the lack of correlation between Darwin and either Broome or Port Hedland ASL. We conclude that poleward "Leeuwin Current" flow is typical over the shelf edge of Port Hedland. Further, the ASL correlation between Port Hedland and Broome suggests that similar conditions prevail eastward to at least 122°E, i.e., over most, if not all, of our study region.

4. Large-Scale Context

[15] To observe large-scale (100 s of km alongshore) patterns, the study began with a three-line CTD survey

(profiling down to at least 600 m in deeper water) and then a seven line SeaSoar survey (reaching only down to about 200 m in deeper water) as the ship returned to the Port Hedland area (Figure 1). Typical station spacing along the CTD lines is about 10 km, while the spacing between successive SeaSoar profiles is about 0.1–2 km, depending on the water depth. For either type of observation, the individual cross-shelf lines are about 200–300 km long, always extending 100–200 km offshore of the 200 m isobath, which we associate with the shelf break. The two sampling modes complement each other because station sampling goes to greater depths, and the SeaSoar obtains far better spatial resolution. Because the CTD and SeaSoar surveys each took about one week to complete, neither is sufficiently synoptic to allow maps to be drawn. On the other hand, we believe that individual sections (which took 1–2 days to complete) are reasonably synoptic. We assume that patterns that appear in both surveys are robust.

[16] The major large-scale trends are demonstrated by the easternmost and westernmost CTD sections (Figures 3 and 4). Both sections share some prominent features. The surface mixed layer, as defined by temperature (difference of 0.1°) or density, is typically about 50–80 m deep, except on the inner shelf where it is shallower. We attribute this deep mixed layer to evaporative effects, whose destabilizing cooling and salinization evidently overcome the stabilizing effect of near-surface radiative heating. All sections show the saltiest water over the inner shelf, with a tendency, over the outer shelf, for the most saline waters to occur near the bottom. Inner shelf waters are typically 0.8 saltier and about 1°–2° cooler than near-surface waters offshore of the shelf break. On a T-S diagram (Figure 5), shelf waters stand out for their correlation of increasing salinity with decreasing temperature. *Shearman et al.* [2004] treat the consequences of evaporation and associated latent heat loss over the inner shelf in more detail. The first CTD and most SeaSoar sections show a pronounced salinity minimum (about 0.2 fresher than ambient waters on section A, Figure 3) in the pycnocline near the shelf break, intersecting the bottom around the 150–250 m isobaths, and then extending offshore at least 80 km. *Holloway* [1995] found a similar salinity pattern near the shelf break that he associated with the Leeuwin Current core.

[17] More equatorward sections (e.g., Figure 4 and near Broome, for example) are clearly fresher than comparable poleward sections near Port Hedland. This is true not only over the shelf, but throughout the sections, down to depths of 200 m or more. If all the waters were moving poleward in the presence of strong surface evaporation, upper ocean waters would become saltier alongshore as we observe. What is striking, however, is that the alongshore salinity gradient extends well below the mixed layer (where the waters have direct contact with the surface): this is especially clear in comparing the T-S diagrams (Figure 5) for different CTD lines. Two mechanisms might account for the alongshore gradation. One would be if fresher waters from the northeast mix horizontally with saltier waters to the southwest. If this were the case, however, we might expect to see some signs, in the form of deeply extending salinity anomalies associated with lateral flow perturbations, of the eddies that carry out the lateral mixing. We do not see such an association. Another possibility is that there is a mechanism by which salinity anomalies generated at the surface are efficiently redistributed both offshore and vertically so as to create this widespread salting. *Brink and Shearman* [2006] propose such a mechanism that depends critically on Ekman convergence in the shelf edge bottom boundary layer (Figure 6).

5. Geostrophy

[18] Much of our understanding of the underway observations is conditioned on the extent to which the flow is geostrophically balanced. For example, geostrophy implies a level of redundancy between density and current fields, and is, in its own right, a diagnostic of the processes taking place. Departures from geostrophy could occur, for example, because of contamination by internal waves and tides, or because the lower-frequency flow itself is ageostrophic because of inertial effects [e.g., *Shearman et al.*, 2000]; see also section 6.2 below. We thus evaluate the extent to which the observed flow is in geostrophic equilibrium with the density field.

[19] Our approach is to calculate the difference between alongshore velocity at depth z and that at a constant reference depth z_0: $\Delta u(y, z) = u(y, z) - u(y, z_0)$, and compare this difference to a similarly referenced estimate of the cross-shelf pressure gradient

$$\Delta p_y(y,z) = p_y(y,z) - p_y(y,z_0) = g \int_{z0}^{z} \rho_y \, dz \qquad (1)$$

so that if the flow is geostrophically balanced,

$$\Delta u(y,z) = -(f\rho_0)^{-1} \Delta p_y(y,z), \qquad (2)$$

where $u(y, z)$ is alongshore velocity, ρ_0 is a constant reference density, $\rho(y, z)$ is the density variation from ρ_0, f is the Coriolis parameter, and subscripts y and z represent partial differentiation with regard to the offshore direction and the vertical coordinate. In the following, Δu will be called the "shear" and $-(f\rho_0)^{-1}\ \Delta p_y(y, z)$ the "thermal wind". The data used for this comparison are the first five shelf edge radiator surveys (the last one being deleted because of its shortened legs, hence lack of comparability). For each section, we average both detided shipboard ADCP data and density into bins that are L wide in the cross-shelf direction. Varying L changes the spatial smoothing. Centered finite differences are then used to compute the thermal wind and shear relative to z_0 = 85 m, a depth chosen to minimize data loss at the shallower ends of the sections. We average groups of binned lines together to create ensemble averages, hence remove some higher-frequency temporal variability (which ought to average out as random noise). For a given 100 km cross-shelf section, about (100/L) −2 shear/thermal wind profiles are available, binned at 2 m (thermal wind) or 8 m (current) vertical intervals. These profiles are then compared via linear correlation c and regression slope a for a single cross-shelf realization or conglomeration. Results are summarized in Table 1 in terms of the means and standard deviations of c and a for a given smoothing.

[20] The comparisons are remarkably unimpressive. For example, with modest smoothing, L = 4 km, the individual

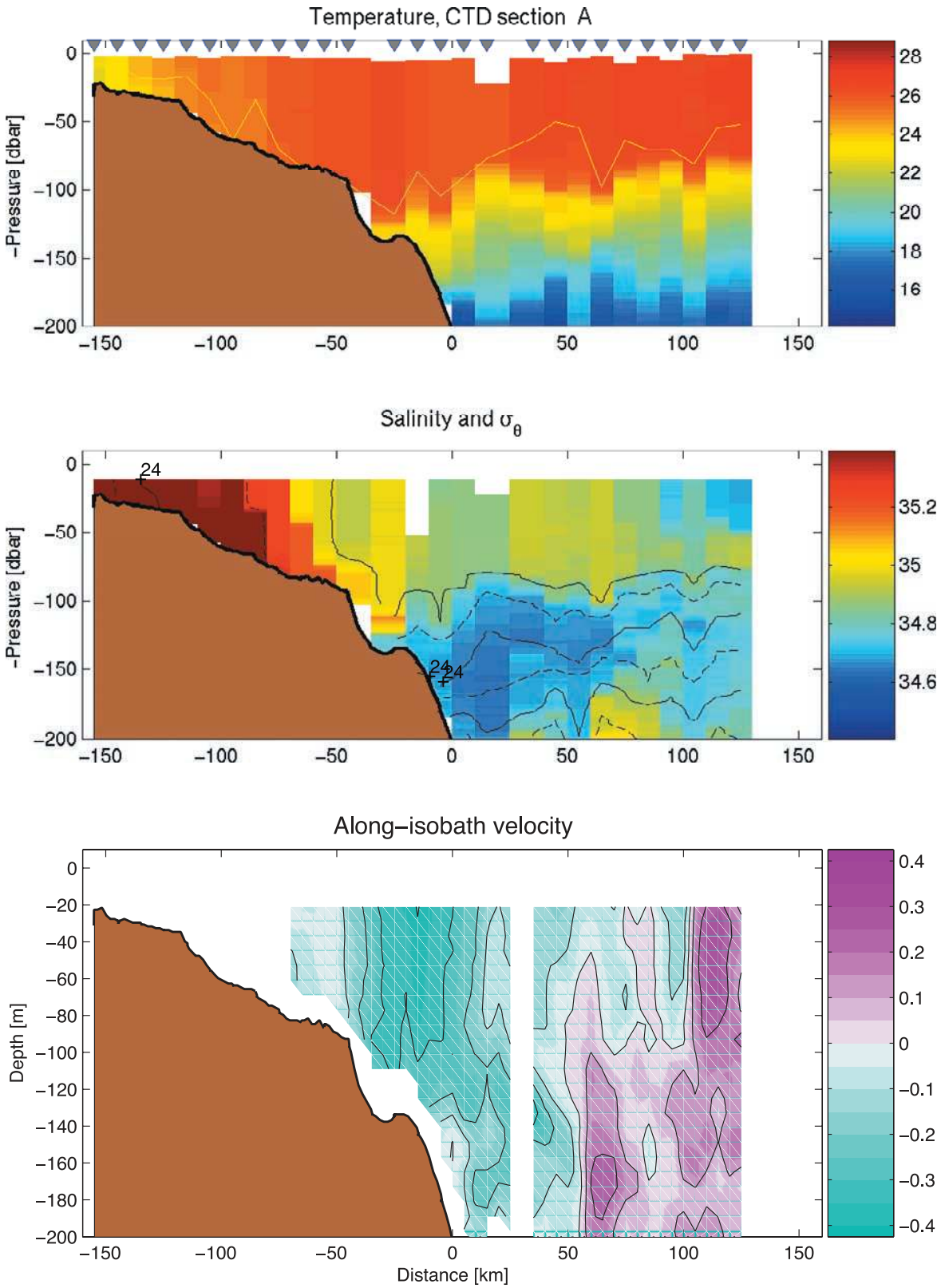

Figure 3. Results from the large-scale CTD survey: temperature, salinity (with density contours overplotted), and alongshore velocity (m/s) on the westernmost line (line A). Positive alongshore flow is toward 29.5° north of east. Only the upper 200 m of data are shown. Mixed layer depth (as defined by a 0.1° temperature difference) is shown as a yellow line.

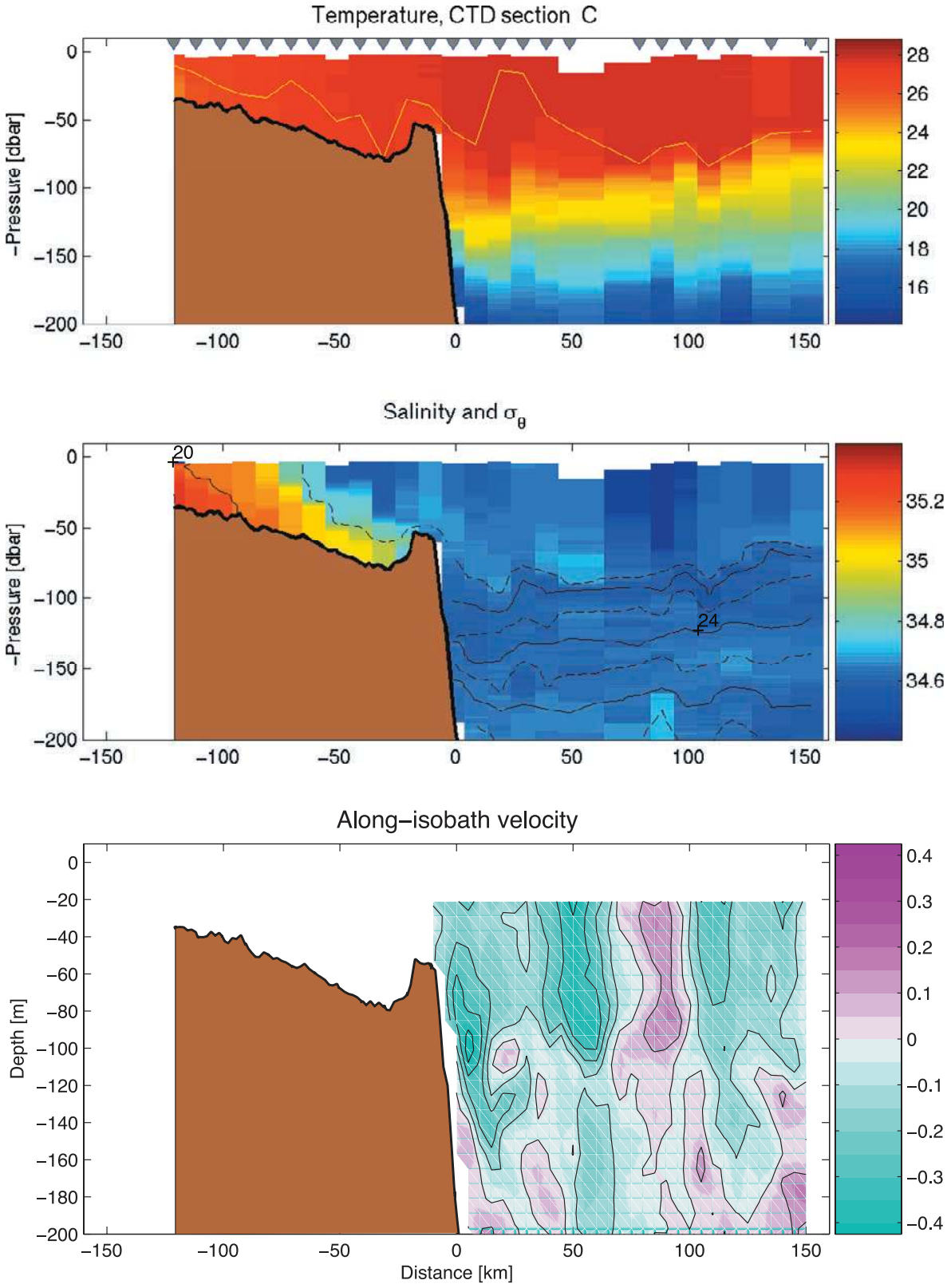

Figure 4. Results from the large-scale CTD survey: temperature, salinity (with density contours overplotted), and alongshore velocity (m/s) on the easternmost line (line C). Positive alongshore flow is toward 29.5° north of east. Only the upper 200 m of data are shown. Mixed layer depth (as defined by a 0.1° temperature difference) is shown as a yellow line.

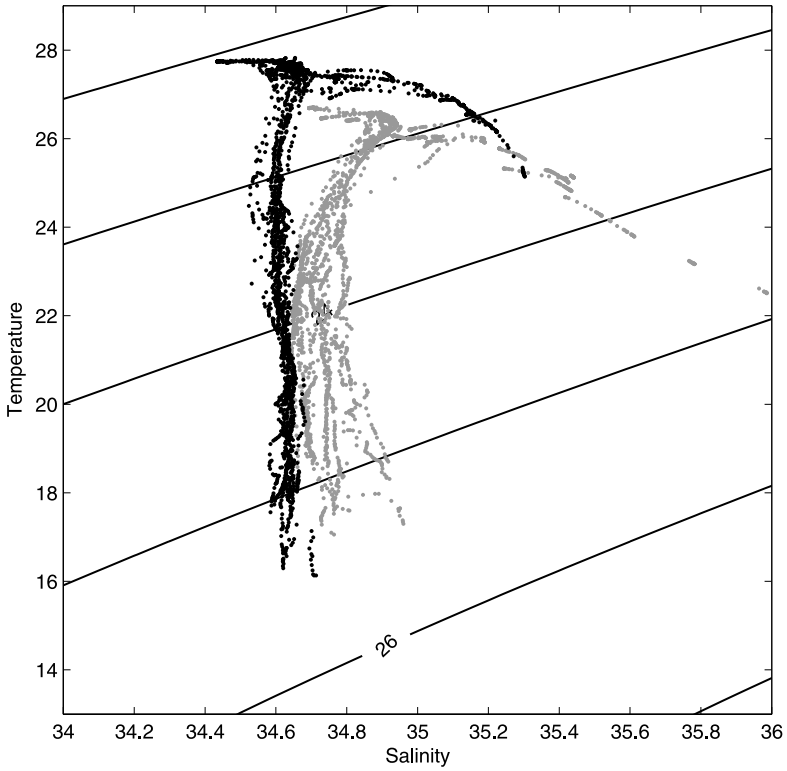

Figure 5. T-S diagram showing all data from the upper 200 m of line A (light dots) and C (dark dots).

sections yield shear-thermal wind correlations ranging between −0.38 and 0.46 (summarized as an average of 0.14, and standard deviation of 0.23: Table 1), while regression slopes range between −0.21 and 0.46 (averaging 0.08). For perfect geostrophy, both c and a are unity. Increased spatial smoothing improves the agreement considerably (Table 1), but even for $L = 16$ km, where the mean correlation improves to 0.56, the range of correlations (standard deviation: 0.28) spans −0.29 to +0.86. For a given amount of spatial smoothing (fixed L), time averaging (in the form of averaging sections together) along the same section improves agreement substantially. Finally, averaging all 20 sections together and using substantial spatial smoothing ($L = 16$ km) leads to much better agreement between thermal wind and shear (mean c, $a = 0.93$, 1.14: very respectable values). Thus, with individual sections and minimal smoothing ($L = 4$ km), the thermal wind equation is not useful for even qualitatively reproducing shears measured with the shipboard ADCP. With substantial spatial smoothing ($L = 16$ km), the agreement of the two shear estimates is usually (but not always) qualitatively useful. Only with substantial spatial smoothing ($L = 8 - 16$ km) and averaging all sections together does the geostrophic shear reproduce actual shears well. For comparison with these scales, the lowest-mode, internal Rossby radius of deformation (which could be an expected natural scale in this system) for the adjoining open ocean is 45 km.

[21] It is possible that the failure of geostrophy on individual sections is due to internal waves. One way to evaluate higher-frequency effects on shears is to compare underway estimates with low-pass-filtered (i.e., internal waves removed) 21–125 m alongshore velocity records from the mooring. This comparison is possible for only

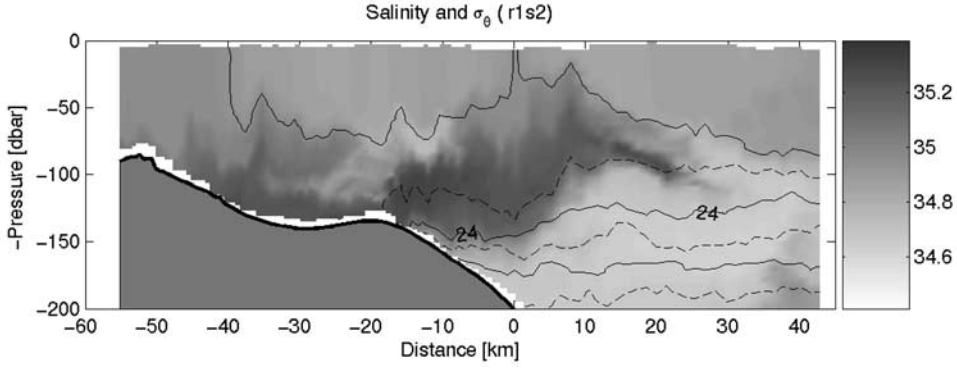

Figure 6. Salinity (shading) and density contours from the first occupation of the second (from the west) line of the repeat mesoscale SeaSoar survey.

Table 1. Thermal Wind Comparison for Repeat Radiator Sections

L, km	Number of Lines	Mean (*c*)	SD (*c*)	Mean (*a*)	SD (*a*)
		Individual Lines			
4	20	.14	.23	.08	.16
8	20	.30	.27	.30	.39
16	20	.56	.28	.89	.72
		Each Radiator Repeat Averaged Together (Four in a Grouping)			
2	5	.30	.15	.12	.07
4	5	.59	.10	.37	.07
8	5	.77	.12	.71	.18
18	5	.76	.30	.90	.40
		All 20 Sections Averaged Together			
2	1	.53	–	.27	–
4	1	.79	–	.60	–
8	1	.87	–	.82	–
16	1	.93	–	1.14	–

five occasions when the ship passed within 3 km of the mooring during the repeat radiators. Again, underway shear and density are averaged into bins of cross-shore width *L*, and then compared to the low-pass-filtered mooring shears. The case by case comparison is generally not good (e.g., Figure 7a is one of the better cases), with RMS differences ranging between 2 cm/s and 8 cm/s. Best agreements between moored and underway Doppler shears occur when $L = 8$ km, and do not seem to depend systematically on the smoothing scale. When all five ship passes are averaged (Figure 7b), agreement improves. We learn from this comparison that the poor case by case agreement implicit in Table 1 cannot be attributed solely to internal wave noise in the underway ADCP current measurements.

[22] We conclude that, with sufficient smoothing (8–16 km in space and some degree of ensemble/time averaging), the thermal wind equation, hence geostrophy, works fairly well in this region. The cause of the case by case disagreement will be revisited in sections 6.2 and 6.4.

6. Mesoscale Surveys

6.1. Overview

[23] On the basis of experience in other regions [e.g., *Gawarkiewicz et al.*, 2004; *Feng et al.*, 2005], we anticipated that the region near the shelf edge would have pronounced mesoscale activity in the form of an unstable, meandering jet with accompanying eddies. We thus designed our repeat sampling to resolve the expected features and their time evolution: the grid is about 100 by 40 km, and is repeated on about a 1.5-day cycle.

[24] The timing of the shelf edge surveys coincides almost exactly with the reversal of the shelf edge current (Figure 2), i.e., with the vanishing of the normal Leeuwin Current. In that sense, our results cannot necessarily be taken to be representative. In some regards, however, the shelf edge variability (Figure 8, 133 m) meets our expectations. The maps show closed, 10–20 km, eddy-like features in density and some jet-like structures in velocity (all velocity data shown in this section have the estimated barotropic tide removed). Our sampling repeat time seems to be well chosen in that, for both temperature and velocity, pattern correlations between maps are about 0.4–0.5 after two repeats (3 days). Thus, although the fields evolve substantially, they change slowly enough to be resolved. Tracking individual temperature, density or current features from map to map does not, however, show any consistent

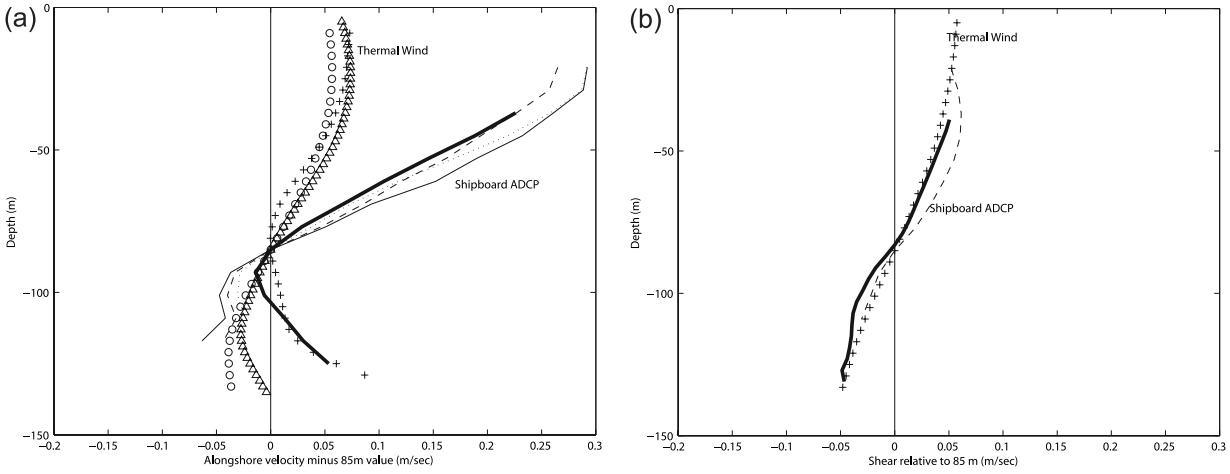

Figure 7. (a) Alongshore velocity relative to 85 m estimated three ways at the location of the current meter mooring on 6 July. The thick solid line represents low-pass-filtered data from the ADCP mooring; thin solid and dashed lines are from averages of shipboard ADCP data; symbols are estimated from the thermal wind equation with different smoothings. Pluses and the thin solid line represent smoothing with $L = 4$ km. Triangles and dots represent smoothing with $L = 8$ km. Circles and the dashed line represent smoothing with $L = 16$ km. (b) Alongshore velocity relative to 85 m estimated three ways at the location of the current meter mooring. The thick solid line represents low-pass-filtered data from the ADCP mooring; thin solid and dashed lines are from averages of shipboard ADCP data. Shown is the average of sections from 30 June and 1, 3, 4, and 6 July sections; $L = 8$ km.

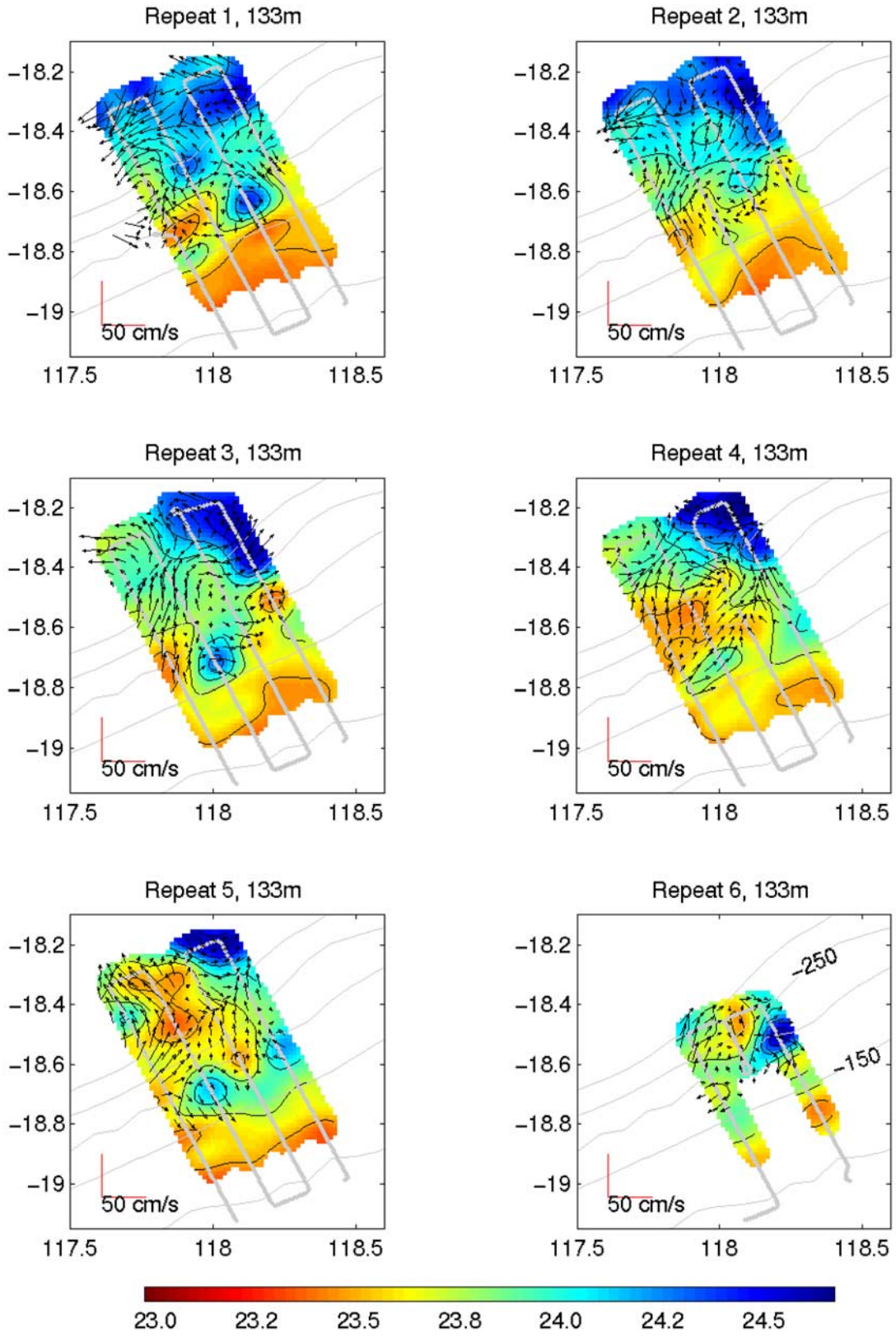

Figure 8. Density (color and contours) and ADCP velocity (vectors) at 133 m depth for all six repeat SeaSoar surveys. The ship track is shown in gray. The 100, 150, 200, 250, and 300 m depth contours are shown.

sense of alongshore propagation as found, for example, south of New England by *Gawarkiewicz et al.* [2004].

[25] The most interesting aspects of the mesoscale results are the surprises. For example, although jets are seen, they do not have the alongshore coherence and consistency found in other shelf break regions. Further, the observed currents do not loop around the density features in the manner that might be expected of a system where the eddy-like features are in nearly geostrophic balance.

6.2. Geostrophy Revisited

[26] The maps provide further means to diagnose the ageostrophy (section 5). First, if the primary ageostrophy is due to time dependence, the temporal acceleration term in geocentric acceleration

$$\boldsymbol{v}_t + f\,\boldsymbol{k} \times \boldsymbol{v} \tag{3}$$

(where $\boldsymbol{v}$ is the velocity vector, $\boldsymbol{v}_t$ is the acceleration vector, and $\boldsymbol{k}$ is the vertical unit vector) ought to be at least comparable to the Coriolis term. We address this possibility two ways. First, we use the repeat maps to estimate the time derivative and Coriolis terms, with map-to-map time steps of 1.5 days for computing accelerations, and by averaging successive maps to obtain the Coriolis terms at the central time. Consistently, and for both the onshore and alongshore equations, the variance (over a map) of the Coriolis term is found to be at least an order of magnitude greater than the acceleration term. Second, we repeat this analysis using the low-pass-filtered moored current meter record. In this case, the cross-shelf acceleration variance is at least an order of magnitude smaller than that of the Coriolis term associated with the alongshore flow. However, the alongshore acceleration and the fv term are quite comparable, and they cancel to some extent. We conclude that time dependence on these scales is not a substantial contributor to the observed ageostrophy of alongshore flow, but that, as in many other shelf settings [e.g., *Allen and Kundu*, 1978], the time dependence is of lowest-order importance in the alongshore momentum equation over the shelf. Thus time dependence may not account for underway alongshore flows not being geostrophic.

[27] The mapped information also allows us to evaluate the importance of inertial effects in the ageostrophy. Specifically, we create maps of the Rossby number

$$R_0 = |(v_x - u_y)|/|f| > 0 \tag{4}$$

for each survey, where the relative vorticity $(v_x - u_y)$ is computed from the mapped (smoothed) fields and is thus likely an underestimate. Although details vary from map to map (Figure 9) and depth to depth, the average R_0 over a map is typically between 0.2 and 0.3, and the maximum R_0 is generally around 1 or slightly higher. Figure 9 can be compared with Figure 8, which shows the velocity and density at the same depth. The importance of nonlinearity is, as expected, highest where the lateral shear or flow curvature is highest, and least at velocity extrema. Clearly, then, advective accelerations are a major contributor to the system's overall ageostrophy. Stated another way, it appears that nonlinearity, rather than time dependence, accounts for the observed failure of geostrophy in the underway measurements.

[28] Earlier results (section 5) show that the agreement of thermal wind and ADCP shear improves somewhat as the data are smoothed in space (L increases). This is consistent with the demonstrated presence of strong nonlinear effects in that smoothing decreases maximum values and spreads out velocity differences over longer scales: both effects tend to reduce the apparent Rossby number. Equivalently, smoothing removes the shortest-scale contributions to shear and thermal wind, and these are presumably the components most strongly affected by the nonlinearity.

6.3. Vertical Structure

[29] Hydrographic features are strikingly depth-dependent. For example, the density structures at 21 m (overplotted with the shallowest, 21 m, underway ADCP velocities: Figure 10) can be compared with the analogous plots at 133 m (Figure 8). The striking thing about the comparison is how dissimilar the features at the two depths are. This point is made more quantitatively using pattern correlations of density (or velocity) at different depths with density (or velocity) at 21 m or 133 m (Figure 11). All of the density fields above 65 m are well correlated with 21 m density, but the deeper fields are not correlated with that at 21 m. Likewise, the fields below about 100 m depth are well correlated with 133 m density, but not with shallow densities.

[30] Thus it appears that structures in the upper 60 m (the surface mixed layer over most of the domain) are uncoupled from features at greater depth. This contrasts with, say, a two-layer baroclinic mode or a continuously stratified low baroclinic mode, where patterns would be correlated with depth, merely having sign reversals at the zero crossings. In these modal cases, the same dynamics would appear over all the depths, but off the northwestern Australia shelf edge, the different depth horizons seem to be genuinely independent.

6.4. Observed Hydrodynamic Stability

[31] The mean density field over the repeat radiators (Figure 12) shows a definite offshore density increase over depths of about 100–150 m, but it decreases offshore over the upper 50 m. The deeper trend is also visible in maps of 133 m density (Figure 8). The tilting isopycnals represent a reservoir of mean potential energy that could conceivably be tapped through baroclinic instability to maintain the offshore eddy field. Physically, the eddies would extract energy from the mean density field by flattening out the isopycnals.

[32] Indeed, there is some qualitative evidence that this energy conversion is taking place. For example, the fifth repeat of the 21 m map (Figure 10, bottom left) shows a patch of dense water near the 200 m isobath (18.7°S, 118.0°E) where the velocity vectors at the center of the feature are oriented offshore at about 0.3–0.5 m/s. This sense of transport (advecting denser water offshore) corresponds to a downgradient flux, and so is consistent with baroclinic instability. A similar, but more poorly resolved, dense patch with offshore advection is also located on map 5 closer to shore (Figure 10), centered at 19.0°S, 118.5°E. Both of these features vanish by 101 m depth. These two examples, both from the same map, are the clearest cases of 21 m density patches corresponding with downgradient eddy density fluxes.

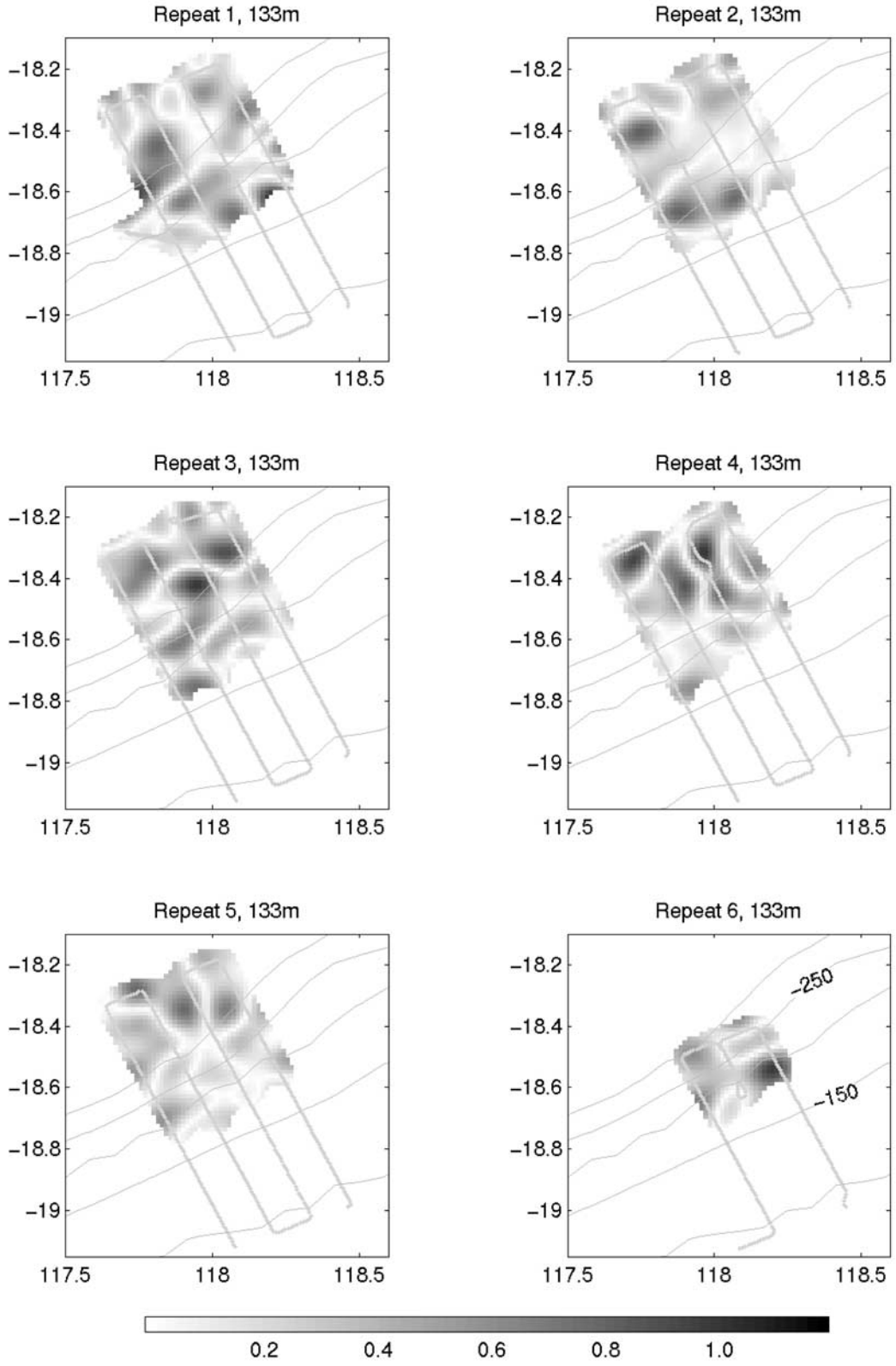

Figure 9. Rossby number at 133 m depth, computed from the velocity data shown in Figure 8.

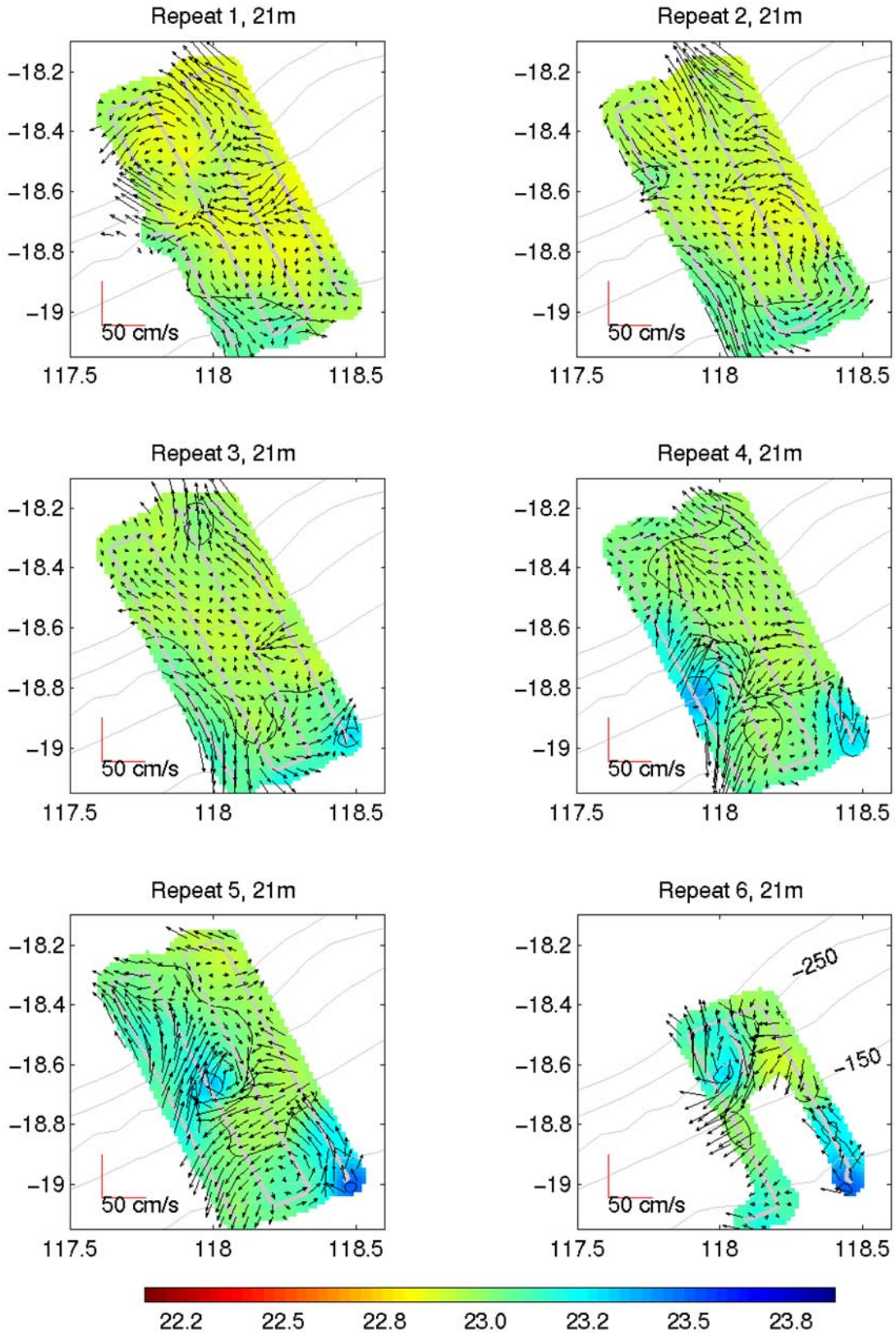

Figure 10. Density (color and contours) and ADCP velocity (vectors) at 21 m depth for all six repeat SeaSoar surveys. The ship track is shown in gray. The 100, 150, 200, 250, and 300 m depth contours are shown.

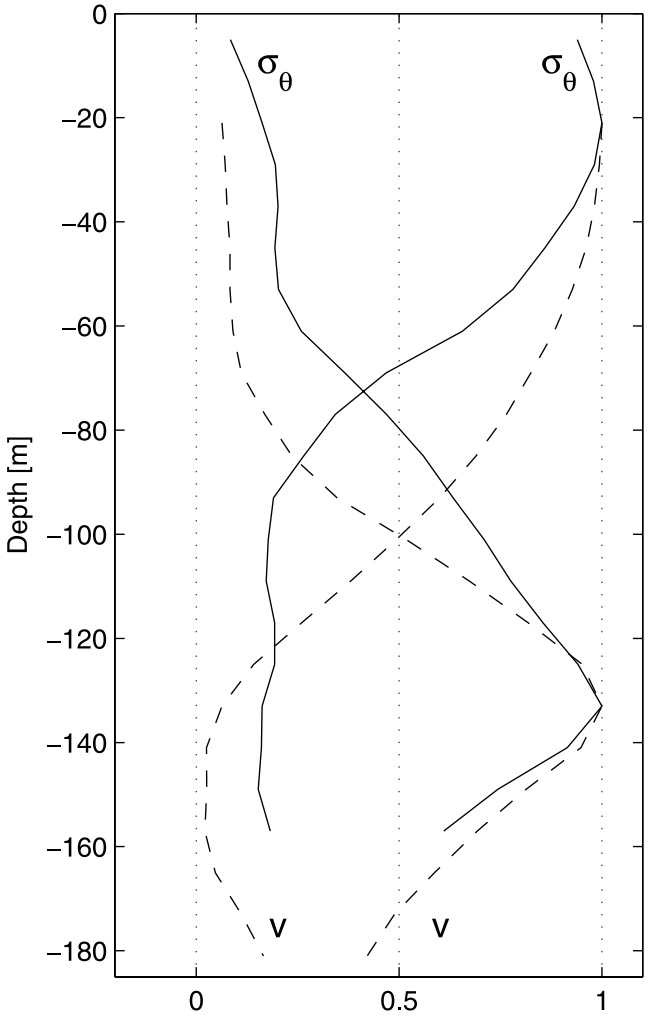

Figure 11. Pattern correlations of density and (complex inner correlation magnitude) velocity as a function of depth. Solid lines are density correlated with 21 and 133 m values. Dashed lines are velocity correlation amplitudes relative to 21 and 133 m.

[33] At 133 m depth (Figure 8), since the mean isopycnals slope upward offshore (opposite to the 21 m situation), onshore eddy density transport corresponds to active instability: many examples of this sort can be found. For example, map 1 has two destabilizing (18.75°S, 17.9°E light; 18.65°S, 118.15°E: dense) features, and one stabilizing (18.5°S, 117.95°E). Further downgradient examples are found on maps 2–5 (a single sustained light feature visible in four successive maps) and 6 (a dense feature).

[34] These qualitative results suggest a net tendency for eddies at both the shallow (21 m) and deeper (133 m) levels to each transport density in their respective downgradient direction. The differing mean gradient directions appear to be qualitatively consistent with the uncoupling of flow at the two depths (section 6.3): each level apparently acts independently to neutralize its own mean offshore gradient.

[35] To gain a better evaluation of the instability processes, we examine the eddy-mean energy conversions for the repeat radiator region. Specifically, the equation governing eddy energy for a nondissipative system (relative to a time/alongshore average) [e.g., *Liang and Robinson*, 2005] is

$$D(K+P)/Dt = C + T + S - (up)_x - (vp)_y - (wp)_z, \quad (5)$$

where $D(\ )/Dt$ is the total (advective) time derivative, the mean potential to eddy potential energy conversion term is

$$C = \langle v\rho \rangle \left(g\rho_{0y}/\rho_{0z} \right), \quad (6a)$$

the barotropic instability mean to eddy conversion is

$$T = -\rho_0 \langle uv \rangle u_{0y}, \quad (6b)$$

and the shear mean to eddy conversion term is

$$S = -\rho_0 \langle uw \rangle u_{0z}. \quad (6c)$$

[36] The eddy kinetic and potential energies are

$$K = \tfrac{1}{2}\, \rho_0 \langle u^2 + v^2 \rangle \quad (6d)$$

and

$$P = -\tfrac{1}{2}\, g \langle \rho^2 \rangle / \rho_{0z}. \quad (6e)$$

[37] The coordinate system is chosen so that y is positive offshore. Angular brackets, $\langle\ \rangle$, denote time/alongshore averages, and the geostrophically balanced mean field is described by $u_0(y,z)$, $\rho_0(y,z)$. The finite amplitude perturbations u, v, w, p, and ρ are defined relative to the $\langle\ \rangle$ mean. This averaging means that terms acting on alongshore gradients, such as $\langle u\rho \rangle$ $(g\rho_{0x}/\rho_{0z})$, do not enter. Dissipative terms omitted from (5) are estimated to be at least about an order of magnitude smaller than the leading terms, given the weak winds in the area and deep mixed layer. Calculations use consistently gridded data from the first five (complete) repeat radiators, and use data only from locations where information was available at all depths from 21 to 181 m (the range being determined by the presence of both current and density information). All results are horizontally averaged layer by layer. The mean fields for our calculation are shown in Figure 13. The $\partial K/\partial t$, $\partial P/\partial t$, C and T terms of (5) could be calculated with confidence from the data set at hand, but alongshore advection and pressure work could not be accounted for.

[38] Results averaged over all five radiators (Figure 13) verify that instability processes are underway. Specifically, the mean-to-eddy potential energy term C is positive at all depths above about 160 m, although it is most substantial between 110 and 150 m depth, and especially shallower than 50 m depth. By comparison, the barotropic instability term T is typically much smaller and is more predominantly negative (indicating a weak, probably insignificant, transfer of energy into the mean kinetic pool). The eddy potential energy P is itself greatest in the 110–150 m and 21–50 m depth ranges, where it is greater than the eddy kinetic energy K by typically a factor 10–20. Further, the (v, ρ) pattern correlation is positive above 120 m (maximum of 0.7, significant at 95% confidence) and negative below

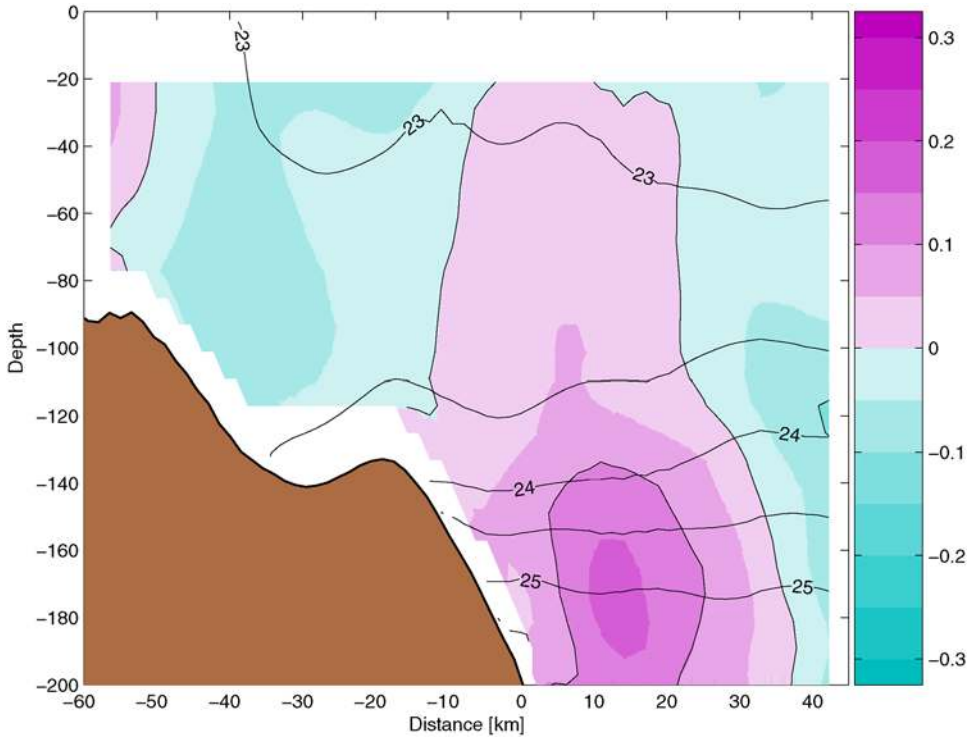

Figure 12. Mean alongshore velocity in m/s (color, positive toward 29.5° north of east) and density (contours) from the average of all 20 lines on the first five (complete) SeaSoar repeat surveys.

(minimum of −0.2). That the shallowest eddy potential energy values should dominate is perhaps not surprising in light of the $(\rho_{0z})^{-1}$ dependence in both P and C, and the typical surface mixed layer depth of 50 m. In the depth ranges where C is most dominant, the ratio P/C, which represents a crude eddy potential energy growth rate, is in the range of 10–15 days.

[39] We also compare the eddy energy transfer term C to the observed local eddy potential energy change $\partial P/\partial t$ (estimated by taking finite differences of averaged P from one map to the next, a 1.5-day time step). At 21 m, for example, the daily estimates of map-averaged $\partial P/\partial t$ ranged between -3.5×10^{-4} to 6×10^{-4} kg/(m s^3), while daily C was always less than 1.2×10^{-4} kg/(m s^3). Thus, on day-to-day timescales, calculated mean to eddy potential energy conversion is far too small to account for the observed eddy potential energy changes. Similarly, the average 21 m $\partial P/\partial t$ over the five repeat radiators is 1.4×10^{-4} kg/(m s^3), while the average C is 0.5×10^{-4} kg/(m s^3). Alongshore advection $u_0 \partial P/\partial x$ and/or pressure work, such as perhaps that associated with alongshore energy propagation, probably dominates local eddy energy changes. The pressure work term could, for example, represent the propagation of eddy energy from an external generation site into the sampling area.

[40] We thus conclude that the system is baroclinically unstable, transferring energy from the mean potential energy pool to the eddy potential energy pool. Similar but independent instabilities appear to be operating in the deep (100–150 m depth) and especially the shallow (shallower than 60 m depth) compartments, each characterized by differing signs of the mean offshore density gradient. The eddy field is highly nonlinear, in the sense that Rossby numbers associated with individual features are as large as O(1), and so the instantaneous flow has a large, even dominant, ageostrophic component. The instability process is, however, regional: changes in observed eddy potential energy within our box clearly require external contributions through propagation or alongshore advection.

6.5. Linear Stability

[41] To explore the stability question further, we consider the linear stability of the mean flow during the repeat mapping period (Figure 12). The model itself is simply a linearization the full adiabatic equations of motion (but with dissipation allowed through a thin bottom boundary layer), and so allows for baroclinic, barotropic, shear and mixed instabilities (see *Brink* [2006] for a detailed description). The model uses realistic background topography and stratification that are independent of the alongshore direction. The geostrophically balanced mean alongshore flow is idealized as Gaussian in shape, described in terms of amplitude, central location (offshore, vertical), and e-folding scales (allowed to differ in the onshore, offshore, up and down directions). Only a single extremum of the mean alongshore flow is allowed, so that a flow with multiple extrema, such as that in Figure 12, cannot be replicated exactly. This is just as well, since it allows the user to isolate effects of the different velocity cores.

[42] First we treat a mean flow centered at 180 m depth over the 350 m isobath with a peak speed of 0.15 m/s. The mean current has a vertical Gaussian decay scale of 120 m (both upward and downward), and a symmetric horizontal

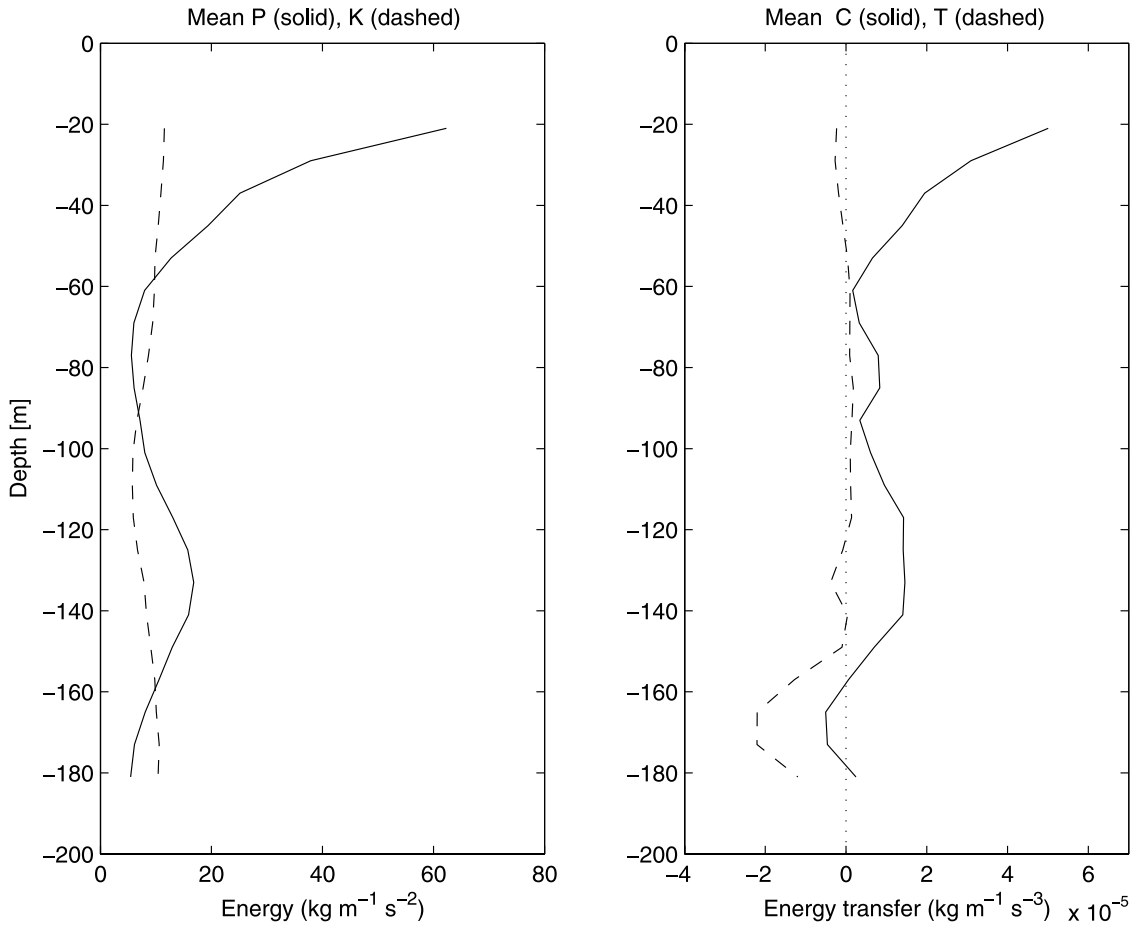

Figure 13. Results from the energy conversion calculations as a function of depth: (left) eddy potential energy (P, solid line) and eddy kinetic energy (K, dashed line) and (right) mean potential to eddy potential energy conversion C (solid line) and mean kinetic to eddy kinetic energy conversion T (dashed line).

scale width of 20 km. This mean current, while it mimics the main aspects of the observed mean flow (Figure 12), has speed monotonically decreasing with height above 180 m, and so is unable to replicate the observed onshore density increase in the upper 50 m (which is treated separately below). The model maximum water depth and domain width are 500 m and 150 km respectively, while 120 horizontal (offshore) and 30 vertically stretched grid points are employed. The most unstable mode has an alongshore wavelength of 18–23 km, an equatorward phase speed of 0.05 m/s and a growth timescale of 12–15 days. The value ranges quoted are those that result from modest variations (typically 10%) in uncertain parameters, such as jet scale width or location, and in grid resolution. The current structure associated with this instability (Figure 14a) is centered on the mean jet at about 180 m depth, and is negligibly weak more than 100 m above or below the jet core. The alongshore flow associated with the unstable wave is highly ageostrophic. The wave's energy is derived about equally from the S and C terms in (5); that is from instability of the vertical shear and from baroclinic instability, respectively. Including a reasonable bottom drag (r = 0.0005 m/s, where (ρr) is the proportionality constant between bottom stress and near bottom alongshore current) makes no difference, since the near-bottom velocities associated with the instabilities are relatively weak. This mode seems to be roughly consistent with the observed finite amplitude unstable flow observed below 120 m in terms of length scales, confinement at depth, and strong ageostrophy.

[43] We also consider the instability of a weak, near surface jet, as might be associated with the observed density variations in the upper 40 m (Figure 12). In this case, the peak mean alongshore flow of 0.025 m/s is centered at the surface, 50 km from the impermeable onshore model boundary. The offshore and onshore scales are both 20 km, and the vertical decay scale is 30 m. In this case, the most unstable wave has an equatorward phase speed of 0.06–0.07 m/s, wavelength of 55–70 km and growth rate of 15–36 days. The instability wave (Figure 14b) appears to be analogous to those found for the Mid Atlantic Bight by *Lozier et al.* [2001], is concentrated in the upper 30 m in and near the jet, and its alongshore flow is typically 70% (by amplitude) geostrophically balanced. Again, the bottom friction plays a negligible role. For this wave, the conversion term C dominates the energy equation (5) by two orders of magnitude relative to T and S: this is clearly a baroclinic instability. This mode agrees roughly with our 21 m observations in terms of length scales and that $C \gg T$.

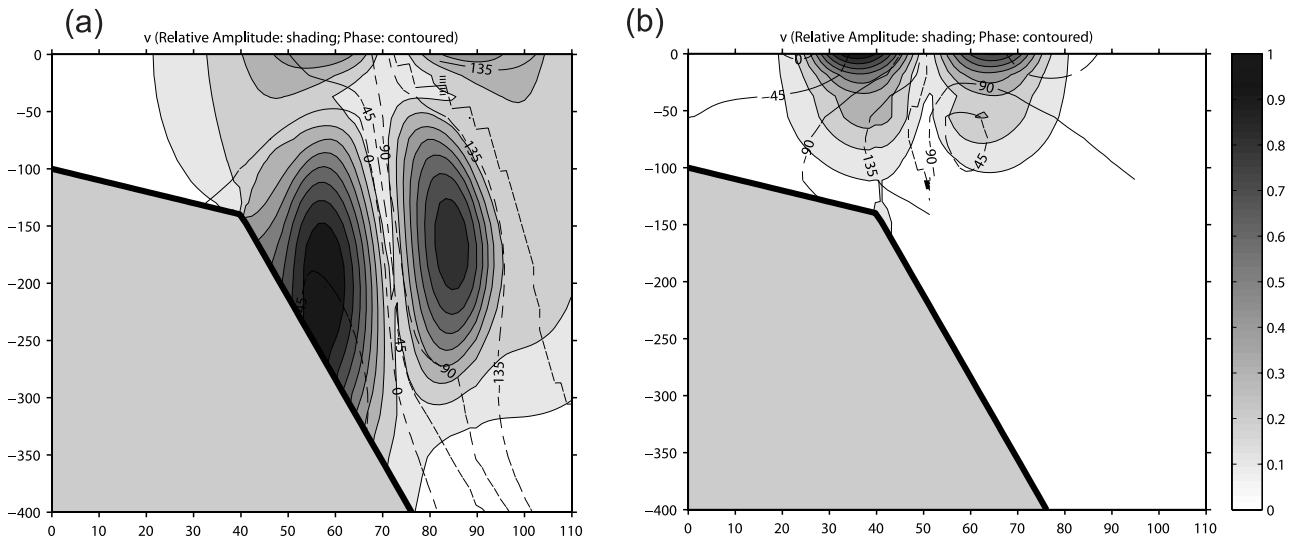

Figure 14. Modal structures (arbitrary amplitude) of the alongshore velocity associated with the most linearly unstable wave mode in the case of two mean flow fields: (a) 0.15 m/s mean flow centered at 180 m depth at x = 70 km and (b) mean flow of 0.025 m/s centered at the surface at x = 50. Note that although the horizontal scale is the same as that of Figure 12, the vertical range is twice that of Figure 12 in order to show the more complete modal structure. Only the innermost 110 km and uppermost 400 m of the model domain are shown.

[44] The linear instability model, while it shows some positive results relative to observations, also has points of disagreement, such as the depth of maximum amplitude in the deep case, or the growth timescales not being as rapid as might be expected given that the eddy field is present immediately after the equatorward alongshore flow is established. The disagreements could have several meanings, including the obvious truth that finite-amplitude instabilities need not resemble the initial instabilities that started them [e.g., *McCreary et al.*, 1991; *Durski and Allen*, 2005]. For example, the observed mean flow (Figure 12) already reflects the adjustments caused by the finite amplitude instability, and so it may have stability properties different from those of an initial equatorward flow. There are insufficient data to conclude whether a similar eddy field existed before the flow reversal, and an exploration of the stability properties of the poleward flow (as estimated from only the first CTD section) does not yield any substantial instabilities. Nonetheless, we believe that the linear stability model does an adequate job rationalizing the observed instabilities in terms of their depth dependence, length scales and ageostrophic flows.

7. Conclusions

7.1. Overview

[45] The northwestern Australian coastal region is characterized by a large-scale tendency for waters at all depths to become saltier poleward (toward the southwest). In normal circumstances, the flow is dominated by the poleward shelf edge Leeuwin Current, which is typically fresher than its surrounding waters, as might be expected given the regional salinity gradients. Analysis of the combined current meter and adjusted sea level data set suggests that the Leeuwin Current is normally present here, but that it has occasional reversals apparently associated with wind forcing.

[46] Repeated, highly resolved 40 × 100 km SeaSoar surveys were carried out near the shelf edge over a 9-day period that, by remarkable chance, coincided with the reversal of the shelf edge flow to an unusual equatorward state. During this period, the overall detided flow was ageostrophic at lowest order, apparently because of inertial effects (the Rossby number averaged 0.2–0.3 over each of the maps, and extreme values were unity or greater). The mapped flow field near the shelf edge was eddy-rich on all surveys, but the patterns observed in the upper 60 m of the water column were independent of those in the deeper 110–160 m horizon. We also find that flow at both levels works to convert mean potential energy into eddy potential energy, but independently. The mean cross-shelf density gradients differ in sign between the two horizons, and so, apparently, two very independent eddy fields form. Energy transformation calculations and linear stability models support this conclusion. To our knowledge, a similar unstable shelf edge flow, that is independently unstable at different depths, has not been observed elsewhere.

7.2. Eddy Scale

[47] *Feng et al.* [2005] study the dynamics of the Leeuwin Current farther poleward (near 29°S), where the coastline tends roughly north–south. They find a rich offshore eddy field, where eddy sizes must be O(100 km) or more in order to be documented by their satellite altimeter data (a 1/3°, roughly 30 km, resolution). This energetic eddy field can be compared to those in the California Current [*Brink et al.*, 2000] and to the Canary Current [*Barton*, 1998]. In all three of these Eastern Boundary current cases, the obvious eddy scale is O(100 km). Although smaller eddies are found off California [e.g., *Washburn and Armi*, 1988], they appear to

be associated with distinct frontal features and they do not seem to be present as consistently. Our repeated, resolved surveys are dominated by eddy energy on shorter, O(10–20 km) scales, although there is some evidence for larger, O(40 km)-scale density variations offshore on three of the seven large-scale SeaSoar survey lines. This latter scale is comparable to the local first-mode internal Rossby radius of deformation of roughly 45 km. Thus our observed small-scale eddy field seems anomalous for an eastern boundary current system.

[48] In contrast, shelf break frontal systems are typified by shorter scales. For example, south of New England in the United States, 10 km eddies are often found associated with the frontal system [e.g., *Garvine et al.*, 1988; *Gawarkiewicz et al.*, 2004], and there is good evidence that these features stem from instabilities on the shelf break front and its associated jet [e.g., *Lozier et al.*, 2001]. In addition to these smaller-scale features, there are much larger warm core rings that are generated far offshore by the Gulf Stream [*Loder et al.*, 1998], but their occurrence near the shelf edge is sporadic.

[49] Thus, in terms of the eddy scale, the northwestern Australian region more nearly resembles a shelf break frontal system than a classical, midlatitude eastern boundary current system. One puzzling aspect, though, is that there is not an obvious front present (Figures 3, 4, and 6). Although at such a low latitude, where the internal Rossby radius is relatively large, one might expect a shelf break front to be less vertically oriented than at higher latitude, the absence is nonetheless striking. However, our energy conversion calculations (section 6.3) demonstrate that there is nonetheless a viable baroclinic energy source. Further, we do not know, on the basis of our data or satellite altimeter data (which only samples scales greater than our 10 km) whether the smaller-scale eddies we observe are typical of the shelf break off northwestern Australia, or whether they are peculiar to times when the shelf edge current is equatorward.

[50] All this raises the question of whether our sampling region should even be expected to resemble a traditional midlatitude eastern boundary current. The present latitude (18°–19°S) is only slightly equatorward of the range typical of eastern boundary currents (roughly 25°–45°). The coastline orientation here (northeast–southwest) is rather oblique compared to the more classical nearly north–south orientation, and this difference could have implications for the offshore propagation of low-frequency (tens of days timescale) information [*Li and Clarke*, 2004]. Although the shelf is relatively wide in our region, it can also be similarly wide in other areas, such as off northwestern Africa. Our northwestern Australian region is characterized by substantial evaporative densification over the shelf, unlike many eastern boundary current regions, but the effect is not strong enough to generate an obvious shelf break front. Perhaps the greatest "anomaly" about the Australian case is the Leeuwin Current, which is the only poleward eastern boundary current. Present thinking has it that the flow is forced by an offshore alongshore pressure gradient that is, in turn, related to the basin-scale circulation and the Indonesian interbasin transfer [e.g., *Church and Craig*, 1998]. However, off western Australia [*Feng et al.*, 2005], where the Leeuwin Current is clearly present, large eddies appear and apparently dominate the eddy field. It is thus not clear to us how one might a priori state what sort of offshore eddy field would be found.

7.3. Eddies, Mean Flow Dynamics, and Cross-Shelf Exchanges

[51] Along the central west coast of Australia (but not all of that coast), the offshore eddy field plays a major role in the mean alongshore momentum balance [*Feng et al.*, 2005]: it acts in the same sense as the alongshore wind stress and opposes the mean alongshore pressure gradient. During our period of intensive observations off northwestern Australia, we found that the eddy field, consistent with baroclinic instability, tends to flatten out the mean isopycnals and so make the mean flow more barotropic. The observed mean to eddy kinetic energy conversion is generally small (Figure 13), so the eddy field apparently does not have an appreciable effect on the strength (as opposed to structure) of the mean alongshore flow. Further, as mentioned above, our intensive sampling did not encompass Leeuwin Current conditions, so we have no information on the role of the eddy field here under typical wintertime conditions. Thus we cannot estimate the importance of the eddy field under normal conditions, but we can say that, during equatorward flow, it was at least important for determining the structure of the alongshore flow.

[52] The eddies we observe do play a clear role in cross-shelf exchanges, since they transport light water onshore in the upper ca. 60 m and denser water offshore below ca. 100 m. In addition, but only during our repeat survey (equatorward flow) period, there is a persistent tongue of salty shelf water separating from the bottom near the 130 m isobath, and then spreading offshore (e.g., Figure 6). *Brink and Shearman* [2006] discuss this feature in more detail, and conclude that it is probably associated with water expelled from the bottom boundary layer onto isopycnal surfaces during equatorward shelf edge flow conditions. During our sampling period, alongshore winds are relatively weak, and so we do not expect that surface Ekman transport played a substantial role. If dissolved nutrient concentrations are higher for denser water (as is often the case in the upper ocean), the eddies and the salt tongue would both contribute to a net pattern of onshore transport of nutrient-depleted water in the upper 60 m (eddy transport) and a net offshore transport below about 100 m (salt tongue and eddies). If these conditions are typical, it is not surprising that this region is one of the least biologically productive continental shelves in the world. However, since intensive (as opposed to extensive) sampling did not occur during normal, Leeuwin Current, conditions, we cannot characterize "normal" conditions other than to say that the salt tongue does not appear to be present.

[53] In total, we conclude that the eddy field plays a significant role in shelf edge processes during our sampling period, and that it is potentially important under more normal, Leeuwin Current, summertime conditions.

[54] **Acknowledgments.** Steve Lentz provided very helpful comments on the manuscript. Shore-based data were kindly made available by Daryl Metters of the Australian National Tidal Centre and Alison Kohout of the Department for Planning and Infrastructure, Freemantle. We appreciate help from Gene Terray and from Eric Firing's group with software for ADCP processing. This work was supported by the Office of

Naval Research Physical Oceanography program, Code 322, grant N00014-02-1-0767. Steve Murray of ONR was particularly helpful.

References

Allen, J. S., and P. K. Kundu (1978), On the momentum, vorticity and mass balance on the Oregon shelf, *J. Phys. Oceanogr.*, *8*, 13–27.

Barton, E. D. (1998), Eastern boundary of the North Atlantic: Northwest Africa and Iberia, in *The Sea*, vol. 11, edited by A. R. Robinson and K. H. Brink, pp. 633–657, John Wiley, Hoboken, N. J.

Beardsley, R. C., R. Limeburner, and L. K. Rosenfeld (1983), Introduction to the CODE-2 moored array and large-scale data report, in *CODE-2: Moored Array and Large-Scale Data Report*, *WHOI Tech. Rep. 85-35*, edited by R. Limeburner, pp. 1–22, Woods Hole Oceanogr. Inst., Woods Hole, Mass.

Brink, K. H. (2006), Coastal-trapped waves with finite bottom friction, *Dyn. Atmos. Oceans*, *41*, 172–190.

Brink, K. H., and R. K. Shearman (2006), Bottom boundary layer flow and salt injection from the continental shelf to slope, *Geophys. Res. Lett.*, *33*, L13608, doi:10.1029/2006GL026311.

Brink, K. H., R. C. Beardsley, J. Paduan, R. Limeburner, M. Caruso, and J. G. Sires (2000), A view of the 1993–1994 California Current based on surface drifters, floats, and remotely sensed data, *J. Geophys. Res.*, *105*(C4), 8575–8604.

Cavlieri, D. J., and S. Martin (1994), The contribution of Alaskan, Siberian and Canadian coastal polynas to the cold halocline layer of the Arctic Ocean, *J. Geophys. Res.*, *99*(C9), 18,343–18,362.

Church, J. A., and P. D. Craig (1998), Australia's shelf seas: Diversity and complexity, in *The Sea*, vol. 11, edited by A. R. Robinson and K. H. Brink, pp. 933–964, John Wiley, Hoboken, N. J.

Clarke, A. J. (1991), The dynamics of barotropic tides over the continental shelf and slope, in *Advances in Tidal Hydrodynamics*, edited by B. B. Parker, pp. 79–108, John Wiley, Hoboken, N. J.

Durski, S. M., and J. S. Allen (2005), Finite-amplitude evolution of instabilities associated with the coastal upwelling front, *J. Phys. Oceanogr.*, *35*, 1606–1628.

Feng, M., S. Wijffels, S. Godfrey, and G. Meyers (2005), Do eddies play a role in the momentum balance of the Leeuwin Current?, *J. Phys. Oceanogr.*, *35*, 964–975.

Firing, E., J. Ranada, and P. Caldwell (1995), Processing ADCP data with the CODAS software system, University of Hawaii technical report, 218 pp., Univ. of Hawaii at Manoa, Honolulu.

Garvine, R. W., K.-C. Wong, G. G. Gawarkiewicz, R. K. McCarthy, R. W. Houghton, and F. Aikman III (1988), The morphology of shelfbreak eddies, *J. Geophys Res.*, *93*(C12), 15,593–15,607.

Gawarkiewicz, G., K. H. Brink, F. Bahr, R. C. Beardsley, M. Caruso, J. F. Lynch, and C.-S. Chiu (2004), A large-amplitude meander of the shelf-break front during summer south of New England: Observations from the Shelfbreak PRIMER experiment, *J. Geophys. Res.*, *109*, C03006, doi:10.1029/2002JC001468.

Holloway, P. E. (1994), Observations of internal tide propagation on the Australian northwest shelf, *J. Phys. Oceanogr.*, *24*, 1706–1716.

Holloway, P. E. (1995), Leeuwin Current observations on the Australian north west shelf, May–June 1993, *Deep Sea Res., Part I*, *42*(3), 285–305.

Li, J., and A. J. Clarke (2004), Coastline orientation, interannual flow, and the strong El Nino currents along Australia's nearly zonal southern coast, *J. Phys. Oceanogr.*, *34*, 2373–2381.

Liang, X. S., and A. R. Robinson (2005), Localized multiscale energy and vorticity analysis. I. Fundamentals, *Dyn. Atmos. Oceans*, *38*, 195–230.

Loder, J. W., B. Petrie, and G. Gawarkiewicz (1998), The coastal ocean off northeastern North America: A large-scale view, in *The Sea*, vol. 11, edited by A. R. Robinson and K. H. Brink, pp. 105–133, John Wiley, Hoboken, N. J.

Lozier, M. S., M. S. C. Reed, and G. Gawarkiewicz (2001), Instability of a shelfbreak front, *J. Phys. Oceanogr.*, *32*, 924–944.

Lueck, R. (1990), Thermal inertia of conductivity cells: Theory, *J. Atmos. Oceanic Technol.*, *7*, 741–755.

McCreary, J. P., Y. Fukamachi, and P. K. Kundu (1991), A numerical investigation of jets and eddies near an eastern ocean boundary, *J. Geophys. Res.*, *96*(C2), 2515–2534.

Pringle, J. M. (2001), Cross-shelf eddy heat transport in a wind-free coastal ocean undergoing winter time cooling, *J. Geophys. Res.*, *106*(C2), 2589–2604.

Shearman, R. K., J. A. Barth, J. S. Allen, and R. L. Haney (2000), Diagnosis of the three-dimensional circulation in mesoscale features with large Rossby number, *J. Phys. Oceanogr.*, *30*, 2687–2709.

Shearman, R. K., K. H. Brink, and F. Bahr (2004), Northwest Australian shelf dynamics experiment: Evaporative dense water formation over the inner-shelf, *Eos Trans. AGU*, *85*(47), Fall Meet. Suppl., Abstract OS33D-03.

Washburn, L., and L. Armi (1988), Observations of frontal instabilities on an upwelling filament, *J. Phys. Oceanogr.*, *18*, 1075–1092.

F. Bahr and K. H. Brink, Woods Hole Oceanographic Institution, Mail Stop 21, Woods Hole, MA 02540, USA. (kbrink@whoi.edu)

R. K. Shearman, College of Oceanic and Atmospheric Sciences, Oregon State University, Corvallis, OR 97331, USA.